

Comparison of energy balance modeling schemes using microwave-derived soil moisture and radiometric surface temperature

William P. Kustas

Hydrology and Remote Sensing Laboratory, U.S. Department of Agriculture-Agricultural Research Service, Beltsville, Maryland, USA

Rajat Bindlish

Science Systems and Applications, Inc., Hydrology and Remote Sensing Laboratory, U.S. Department of Agriculture-Agricultural Research Service, Beltsville, Maryland, USA

Andrew N. French¹ and Tom J. Schmugge

Hydrology and Remote Sensing Laboratory, U.S. Department of Agriculture-Agricultural Research Service, Beltsville, Maryland, USA

Received 3 April 2002; revised 15 April 2002; accepted 15 April 2002; published 20 February 2003.

[1] A Two-Source (soil + vegetation) Energy Balance (TSEB) modeling scheme has been developed to use either microwave-derived near-surface soil moisture (TSEB_{SM}) or radiometric surface temperature (TSEB_{TR}) as the key remotely sensed surface boundary condition for computing spatially distributed heat fluxes. Output of the surface heat fluxes from both two-source schemes have been validated using tower- and aircraft-based flux observations. However, these observations rarely provide the necessary spatial information for evaluating heat flux patterns produced by spatially based models. By collecting microwave and radiometric surface temperature observations concurrently during the Southern Great Plains 1997 (SGP97) experiment conducted in Oklahoma, USA, heat flux estimates by the two modeling schemes were compared on a pixel-by-pixel basis. This provided a unique opportunity for evaluating the consistency in spatial patterns of the heat fluxes. Comparisons with radiometric surface temperature observations helped to elucidate factors contributing to discrepancies between TSEB_{SM} and TSEB_{TR} output, because the TSEB_{SM} modeling scheme computes an effective surface temperature. Results from the heat flux comparisons and simulated versus observed surface temperatures suggested revisions to TSEB_{SM} parameterizations are needed to better constrain flux predictions from the soil and vegetation. When the revisions are made, TSEB_{SM} accommodates a wider range of environmental conditions. The revisions involve an adjustment to the soil evaporation algorithm for differential drying of the near-surface soil layer and adopting the Priestley–Taylor coefficient estimated from the TSEB_{TR} model. It was also found that areas with high fractional vegetative cover conditions, TSEB_{TR} estimates of energy partitioning between sensible and latent heat flux at the soil surface (expressed in terms of the soil Bowen ratio, B_{OS}), were uncorrelated to the remotely sensed near-surface soil moisture. This contributed to inconsistencies in B_{OS} patterns estimated by TSEB_{TR} during a dry down period. A ~20% change in the maximum fractional vegetation cover estimated using the remote-sensing-based algorithm is shown to dramatically impact B_{OS} values estimated by TSEB_{TR} for the densely vegetated areas while having little effect on TSEB_{SM}-derived values. This result suggests that under certain environmental conditions, energy balance partitioning at the soil surface over densely vegetated areas may be tenuous using the TSEB_{TR} scheme. *INDEX TERMS:* 3360 Meteorology and Atmospheric Dynamics: Remote sensing; 1818 Hydrology: Evapotranspiration; 1866 Hydrology: Soil moisture; 3322 Meteorology and Atmospheric Dynamics: Land/atmosphere interactions; *KEYWORDS:* remote sensing, energy balance modeling, radiometric surface temperature, microwave soil moisture, model comparisons

¹Now at Hydrological Sciences Branch, NASA Goddard Space Flight Center, Greenbelt, Maryland, USA.

Citation: Kustas, W. P., R. Bindlish, A. N. French, and T. J. Schmugge, Comparison of energy balance modeling schemes using microwave-derived soil moisture and radiometric surface temperature, *Water Resour. Res.*, 39(2), 1039, doi:10.1029/2002WR001361, 2003.

1. Introduction

[2] The Two-Source Energy Balance (TSEB) model designed to use remotely sensed (radiometric) surface temperature (TSEB_{TR}) and remotely sensed (microwave-derived) near-surface soil moisture (TSEB_{SM}) have been applied to data collected during the Southern Great Plains 1997 (SGP97) experiment. For TSEB_{TR}, TIMS (Thermal Infrared Multispectral Scanner) radiometric surface temperature data at high resolution (~12 m pixel) have been used [French *et al.*, 2000]. For TSEB_{SM}, the L-band ESTAR (Electronically Scanned Thinned Array Radiometer) near-surface soil moisture (~0–5 cm layer) product at 800 m pixel resolution has been applied [Kustas *et al.*, 2001]. Computed heat fluxes from both modeling schemes have been validated using tower- and aircraft-based flux observations from SGP97 study sites. Results of the comparisons between flux observations and model estimates suggest discrepancies of 20–30% can be expected.

[3] Tower-based flux observations represent a very small fraction of the land surface, while aircraft-based flux measurements provide regional scale averages. Although such comparisons provide a level of confidence in model heat flux estimates, it is nearly impossible to validate the spatial patterns in heat flux produced by such models over a landscape [e.g., Mecikalski *et al.*, 1999; Jiang and Islam, 2001]. In order to gain more insight into the uncertainty in spatially distributed fluxes from such models, there is a need for studies that compare output from various spatially based models on a pixel-by-pixel basis.

[4] For two days, (Days 182 and 183, 1–2 July 1997) both TIMS and ESTAR data were collected during the same midmorning period (~1630–1700 UTC) over the El Reno study site. This provided a unique opportunity to compare output from two different model formulations for the same region on a pixel-by-pixel basis. The TIMS-derived 12 m resolution radiometric surface temperature, $T_R(\theta)$, (where θ is the sensor viewing angle; see Norman *et al.* [1995]) data were aggregated to the same 800 m pixel resolution of the ESTAR data. In addition, since TSEB_{SM} also simulates an effective surface temperature, T_{surf} , these estimates were compared to $T_R(\theta)$ observed from TIMS. This comparison provided additional information for determining the TSEB_{SM} model formulations needing revisions in order to obtain better agreement between observed and simulated surface temperature and reduce discrepancies in heat flux output with TSEB_{TR}.

2. Methodology

[5] Both the TSEB_{TR} and the TSEB_{SM} models use the land surface transfer scheme developed by Norman *et al.* [1995]. A series resistance network for the vegetation and soil components (Figure 1) is utilized based on the approximation that the radiometric and effective surface temperature comprises a mean canopy, T_C , and soil, T_S , component temperature

$$T_{surf} \approx T_R(\theta) \approx (f_C(\theta)T_C^4 + (1 - f_C(\theta))T_S^4)^{1/4} \quad (1)$$

where the fractional canopy (vegetation) cover, f_C , which will vary depending on radiometer viewing angle θ [Norman *et al.*, 1995], is estimated from simple relation to a “normalized” or rescaled Normalized-Difference-Vegetation-Index (NDVI) as defined by Choudhury *et al.* [1994].

$$f_C = 1 - N_*^p \quad (2)$$

with

$$N_* = \frac{NDVI_M - NDVI}{NDVI_M - NDVI_O} \quad (3)$$

and p ranges from ≈ 0.5 to 0.7 for a dark and bright soil, respectively. In the present study, equations (2)–(3) were used with $p = .625$, $NDVI_O = 0$, $NDVI_M = 0.7$. The sensible heat fluxes from the canopy, H_C , and soil, H_S , are initially estimated using the following relations,

$$H_C = \rho C_P \frac{T_C - T_{AC}}{R_B} = \left(1 - f_G \alpha_{PT} \left[\frac{\Delta}{\Delta + \gamma} \right]\right) R_{N,C} \quad (4a)$$

$$H_S = \rho C_P \frac{T_S - T_{AC}}{R_S} \quad (4b)$$

$$H = H_C + H_S = \rho C_P \frac{T_{AC} - T_A}{R_A} \quad (4c)$$

where ρ is the air density, C_P is the heat capacity of air, α_{PT} is the Priestley–Taylor parameter set equal to 1.3 [Priestley and Taylor, 1972] for the green part of the canopy, Δ is the slope of the saturation vapor pressure–temperature curve at T_C , γ is the psychrometric constant, f_G is the fraction of the canopy that is “green” or actively transpiring, which may be obtained from knowledge of the phenology of the vegetation, and $R_{N,C}$ is net radiation of the canopy component. The resistances R_B , R_S and R_A are the total boundary layer resistance of the complete canopy of leaves, the soil surface aerodynamic resistance and the aerodynamic resistance to heat transfer from canopy air space temperature, T_{AC} , to the surface layer air temperature, T_A , respectively.

[6] The resistances are estimated from formulas described by Norman *et al.* [1995] with modifications suggested by Kustas and Norman [1999, 2000b]. The net radiation of the canopy originally estimated using an exponential decay with depth as a function of the fractional vegetation cover or leaf area index [Norman *et al.*, 1995], has been replaced with a more physically based radiation extinction model where shortwave and longwave exchanges are evaluated within the canopy layer [Kustas and Norman, 1999]. Justification for the Priestley–Taylor assumption used in equation (4a) is given by Norman *et al.* [1995]. However, it is important to note that the Priestley–Taylor formulation only provides an initial calculation. It can be overridden to accommodate a wider range of environmental conditions, such as if the temperature difference between the soil–canopy system and the atmosphere is large causing erro-

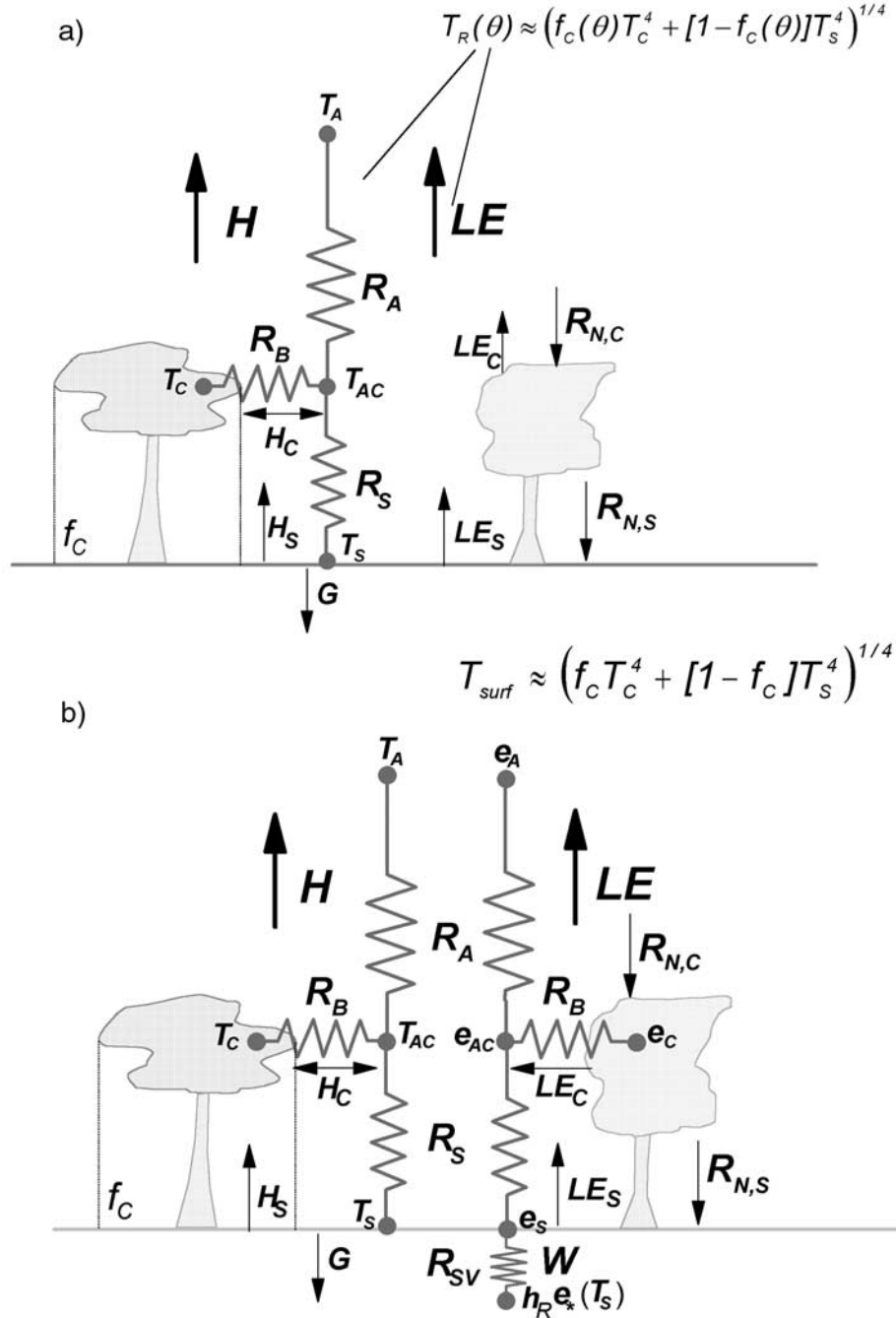


Figure 1. Schematic illustrating resistance network for a) TSEB_{TR} modeling scheme and b) TSEB_{SM} modeling scheme. For definition of symbols see text.

neous flux estimates (e.g., condensation during the daytime period). An iteration procedure has been recently developed [Kustas and Norman, 2000a, 2000b; Kustas et al., 2003] which will adjust α_{PT} until values of T_C and T_S used in equation (1) agree with the measured $T_R(\theta)$.

[7] For TSEB_{SM} a similar set of expressions are used, except the soil surface latent heat flux is solved directly from the expression,

$$LE_S = \frac{\rho C_P}{\gamma} \frac{h_R e_*(T_S) - e_{AC}}{R_{SV} + R_S} \quad (5)$$

where the resistance R_{SV} represents the surface soil resistance to water vapor transfer within the soil layer. This is estimated from an exponential expression relating R_{SV} to the ratio of actual near-surface (viz., 0–5 cm layer) soil water content derived from the microwave data to saturated soil water content based on soil texture information [Sellers et al., 1992]. The parameter $e_*(T_S)$ is the saturation vapor pressure at soil surface temperature T_S , e_{AC} is the vapor pressure in the canopy air space, and h_R is the relative humidity of the soil layer computed from the surface soil water content using the method described by Camillo and

Gurney [1986]. With the expression for H_S in equation (4b) and taking soil heat flux as a fraction of net radiation at the soil surface, namely $G \approx 0.3R_{N,S}$ [Norman *et al.*, 1995], the soil surface energy balance (i.e., $R_{N,S} - G - LE_S - H_S = 0$) can be satisfied; this yields a soil surface temperature, T_S . Then with T_C derived from the Priestley–Taylor formulation (equation (4a)), both T_S and T_C are used in deriving the effective surface temperature T_{surf} using equation (1). The vapor pressure of the canopy surface, e_C required to achieve balance for the canopy layer (i.e., $R_{N,C} - H_C - LE_C = 0$) is again solved via the Priestley–Taylor expression for the vegetation, where

$$LE_C = \frac{\rho C_P}{\gamma} \frac{e_{AC} - e_C}{R_B} = f_{G\alpha_{PT}} \left[\frac{\Delta}{\Delta + \gamma} \right] R_{N,C} \quad (6)$$

Unfortunately, adjusting α_{PT} in the Priestley–Taylor formulation for a wider range of environmental conditions is not as straight forward with the TSEB_{SM} scheme since equation (1) cannot be used to restrict the component temperatures as with TSEB_{TR}. However, the model will not permit nonphysical solutions, such as $LE_s < 0$ or condensation during the daytime. In this case, the Priestley–Taylor approximation is dropped, and several approximations are used; see Kustas *et al.* [2001] for further details concerning this issue.

3. Data

[8] Details of the SGP97 study area and the experiment, including the processing of the ESTAR data, are given by Jackson *et al.* [1999] and on the World Wide Web (<http://hydrolab.arsusda.gov/sgp97/>). This region is well instrumented for hydrometeorological research. The region contains a relatively dense network of meteorological stations, the Oklahoma Mesonet [Brock *et al.*, 1995], and flux towers, which were in operation during the SGP97 field campaign [Twine *et al.*, 2000].

[9] The L-band passive microwave data were collected using the Electronically Scanned Thinned Array Radiometer (ESTAR) flown by the P-3 aircraft operated by NASA's Wallops Flight Center. ESTAR observations were made over a 30 day period from 18 June Day of Year (DOY) 169 to 17 July DOY 198. The instrument was installed to provide horizontally polarized data. Experiments, such as Washita '92 at the watershed scale and SGP97 at the regional scale, have demonstrated the reliability of this instrument [Jackson *et al.*, 1995, 1999].

[10] The TIMS instrument [Palluconi and Meeks, 1985], a six channel scanner operating in the thermal infrared (8 to 12 μm) region of the electromagnetic spectrum, was flown on a DOE Cessna Citation aircraft. Data collection focused on one of the main study sites, El Reno, which contained a relatively dense network of flux stations. The TIMS provided radiometric surface temperature observations at ≈ 12 m pixel resolution with viewing angles ranging from nadir (i.e., $\theta = 0^\circ$) to $\theta \approx 25^\circ$; hence, the average sensor viewing angle for the $T_R(\theta)$ observations was on the order of 10° . From the same aircraft, the Thematic Mapper Simulator (TMS) instrument provided similar resolution visible-near infrared imagery for creating an NDVI map for the area. The El Reno flight lines provided coverage of an area approximately 8 km north–

Table 1. Meteorological Conditions (Half-Hourly Average Values) During the Aircraft Overpass From Mesonet Station Observations Located Within the El Reno Area

DOY	Time, CST	Air Temperature, °C	Relative Humidity, %	Wind Speed, m s ⁻¹	Solar Radiation, W m ⁻²
182	1100	31.6	58	6.8	890
183	1030	31.0	59	2.4	820

south by 28 km east–west, which was primarily composed of harvested winter wheat fields and grasslands used for grazing cattle. French *et al.* [2000] provide further details concerning the processing of these data, including correction for atmospheric effects. Both NDVI and $T_R(\theta)$ were aggregated to 800 m pixel resolution using radiances to allow comparison of output between TSEB_{TR} and TSEB_{SM}.

[11] A land cover classification required for estimating surface roughness and vegetation parameters was taken from an analysis performed by Doraiswamy *et al.* [1998] using a Landsat TM (Thematic Mapper) scene and on site surveys as part of a supervised approach. A soil texture database used for estimating soil matric potential and h_r was derived from the State Soil Geographic Database (STATSGO) developed by the USDA Natural Resources Conservation Service (NRCS). One of the products available is a soil texture classification of the surface soil on a 1 km grid, which was resampled to the 800 m grid.

[12] Meteorological data, which included screen level air temperature and relative humidity, wind speed, and incoming solar radiation were defined for each 800 m pixel using the Mesonet network [Kustas *et al.*, 2001]. The wind speed observations were available at 10 m above ground level (agl) and air temperature/relative humidity at 1.5 m agl. Details of the measurements and quality control of the data is described by Shafer *et al.* [2000].

[13] The two-day sequence of microwave and thermal-IR surveys followed a heavy rainfall event (~ 6 cm) that occurred over the El Reno area on DOY 179. A general drying trend followed for the next several days, although there was a brief shower on DOY 181 adding 0.75 cm of precipitation. In Table 1 is a list of general meteorological conditions existing around the time of the aircraft coverage. The greatest difference in meteorological conditions between the two overflights is the wind speed, which was relatively light for DOY 183 ($u \sim 2.5$ m s⁻¹) compared to DOY 182, where $u \sim 7$ m s⁻¹. Higher surface soil moisture conditions existed in the region on DOY 182, particularly with the additional precipitation falling the day before.

4. Results

[14] Both the TSEB_{SM} and TSEB_{TR} schemes were run using half-hourly averaged meteorological data from the Mesonet network. Overlapping coverage for ESTAR and TIMS/TMS comprised an area approximately 6 km north–south by 20 km east–west. Approximately 1/4 of the domain on the west end was primarily composed of harvested winter wheat fields (either in stubble or tilled bare soil), while the remaining 3/4 of the area consisted of pasture/grasslands and crops.

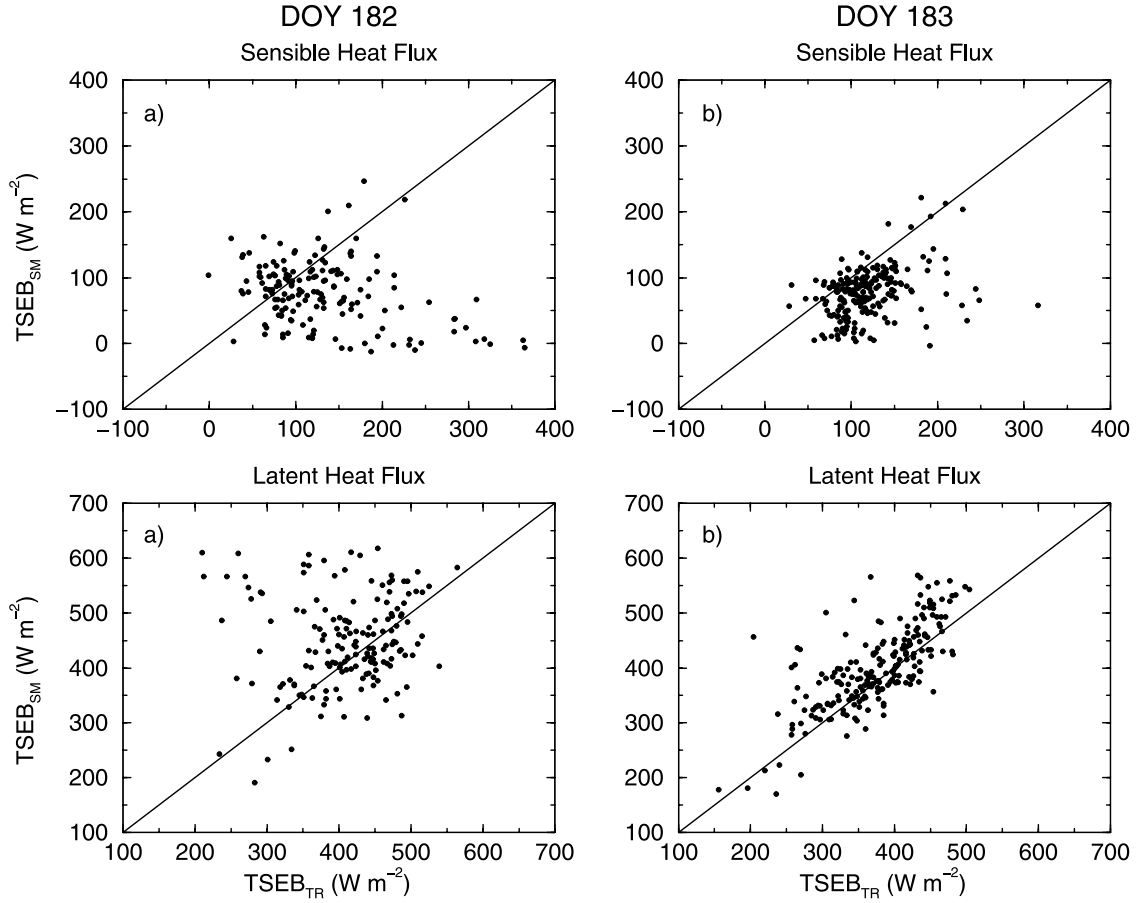


Figure 2. Comparison of sensible(H), and latent (LE) heat fluxes between original $TSEB_{SM}$ scheme and the $TSEB_{TR}$ formulation for a) DOY 182 and b) DOY 183 overpass.

[15] Since the largest discrepancies between the two models are with the turbulent fluxes, H and LE , and not R_N and G , the results only for the turbulent fluxes will be presented here. A pixel-by-pixel comparison of H and LE for DOY 182 (Figure 2a) shows significant scatter having Root-Mean square-Difference (RMSD [Willmott, 1982]) of $\sim 110 \text{ W m}^{-2}$ for both H and LE . The area-average $\langle H \rangle$ from $TSEB_{SM} \approx 50 \text{ W m}^{-2}$ lower and $\langle LE \rangle \approx 40 \text{ W m}^{-2}$ higher than estimated by $TSEB_{TR}$ (Table 2). T_{surf} simulated

by $TSEB_{SM}$ yields a mean bias (underestimate) of $\approx 1.3 \text{ K}$ (Table 2), with an RMSD $\approx 3 \text{ K}$ from the pixel-by-pixel comparison (Figure 3a). In comparison to DOY 182, the pixel-by-pixel comparison of H and LE for DOY 183 shows less scatter (Figure 2b) yielding an RMSD of $\sim 60 \text{ W m}^{-2}$ for H and LE . The area-average $\langle H \rangle$ from $TSEB_{SM} \approx 40 \text{ W m}^{-2}$ lower and $\langle LE \rangle \approx 25 \text{ W m}^{-2}$ higher than estimated by $TSEB_{TR}$ (see Table 2). The pixel-by-pixel comparison of T_{surf} simulated by $TSEB_{SM}$ with $T_R(\theta)$ from TIMS indicates

Table 2. Comparison of Area-Average Sensible, $\langle H \rangle$, and Latent Heat Fluxes, $\langle LE \rangle$, Soil Surface Bowen Ratios, $\langle B_{OS} \rangle$, and Aerodynamic Resistance From Air–Canopy, $\langle R_A \rangle$, and the Soil Surface Layer, $\langle R_S \rangle$, Estimated by the Two Models^a

Model	DOY 182			DOY 183		
	$TSEB_{TR}$	$TSEB_{SM}$ (Original)	$TSEB_{SM}$ (Revised)	$TSEB_{TR}$	$TSEB_{SM}$ (Original)	$TSEB_{SM}$ (Revised)
$\langle H \rangle, \text{W m}^{-2}$	131	78	126	119	77	113
$\langle LE \rangle, \text{W m}^{-2}$	407	449	393	374	400	351
$\langle T_R(\theta) \rangle, ^\circ\text{C}$	37.0	37.0	37.0	40.1	40.1	40.1
$\langle T_{surf} \rangle, ^\circ\text{C}$	—	35.7	37.1	—	38.1	40.3
$\langle B_{OS} \rangle = \langle H_S \rangle / \langle LE_S \rangle$	0.89	0.63	1.0	1.25	0.70	1.31
$\langle R_A \rangle, \text{s m}^{-1}$	15	15	15	30	30	29
$\langle R_S \rangle, \text{s m}^{-1}$	78	78	77	111	109	108

^aIn addition, a comparison between $TSEB_{SM}$ -derived area-average surface temperature, $\langle T_{surf} \rangle$, versus remotely sensed (radiometric) surface temperature, $\langle T_R(\theta) \rangle$, is given.

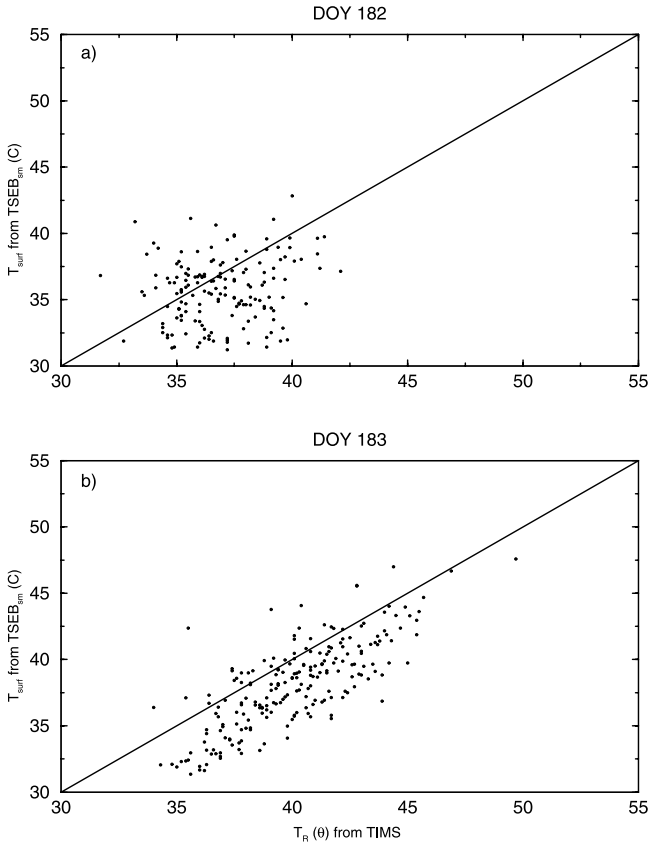


Figure 3. Comparison of effective surface temperature (T_{surf}) simulated by the original TSEB_{SM} formulation versus remotely sensed (radiometric) surface temperature ($T_R(\theta)$) from the TIMS instrument for a) DOY 182 and b) DOY 183 overpass.

a similar scatter to DOY 182 results with an RMSD ≈ 3 K (Figure 3b), but a greater bias (underestimate) ≈ 2 K (see Table 2).

[16] Previous studies comparing T_{surf} simulated by TSEB_{SM} with $T_R(\theta)$ from ground and aircraft observations show a similar scatter, albeit without a significant bias [Kustas et al., 1999, 2001]. The fact that $\langle T_{\text{surf}} \rangle$ is less than $\langle T_R(\theta) \rangle$ is not surprising, however, since $T_R(\theta)$ is affected by surface moisture conditions whereas the TSEB_{SM} formulation uses an integrated soil moisture value for the 0–5 cm depth. Indeed, Capehart and Carlson [1997] using a soil profile model show a significant “decoupling” between surface soil moisture (≈ 0.5 cm) and the moisture at 5 cm as the soil dries suggesting that the soil surface energy balance becomes more strongly coupled to surface moisture conditions than at deeper layers as the soil dries.

[17] This decoupling may also significantly contribute to the scatter in computed H and LE between TSEB_{SM} and TSEB_{TR}. In particular, the partitioning of the available energy at the soil surface ($R_{N,S} - G$) between H_S and LE_S is likely to be significantly different between the two modeling schemes. Bowen ratio values at the soil surface ($B_{OS} = H_S/LE_S$) computed from the output of the two models were compared (Figure 4) as a function of the ratio of the ESTAR-derived soil moisture, W , to the saturated water content values, W_S , determined from soil texture

information [Rawls et al., 1992]. The plots indicate significant differences exist between the two modeling schemes with the output from TSEB_{TR} showing virtually no correlation with relative near-surface soil moisture conditions (as defined by W/W_S) and a greater range in B_{OS} values. For both days, area-average B_{OS} , $\langle B_{OS} \rangle = \langle H_S \rangle / \langle LE_S \rangle$, from TSEB_{SM} was less than TSEB_{TR}, reaching almost 1/2 the $\langle B_{OS} \rangle$ value from TSEB_{TR} on DOY 183 (Table 2).

[18] Although $\langle B_{OS} \rangle$ computed by TSEB_{TR} is lower on DOY 182, nearly 20% of the pixels have $B_{OS} \geq 10$ with almost 25% of the pixels having $B_{OS} \geq 5$. For DOY 183, only $\sim 1\%$ of the pixels computed by TSEB_{TR} have $B_{OS} \geq 10$ and increases only to $\sim 10\%$ of the pixels having $B_{OS} \geq 5$. This significant change in the distribution of B_{OS} values as the soil surface dries suggests there is an inconsistency in the TSEB_{TR} output of energy partitioning at the soil surface. This will be investigated in greater detail below.

[19] The larger $\langle B_{OS} \rangle$ values estimated by TSEB_{TR} and the results comparing T_{surf} simulated by TSEB_{SM} with $T_R(\theta)$ from TIMS (Figure 3) suggest that differential drying in the soil surface layer existed, leading to the decoupling effect described by Capehart and Carlson [1997]. An attempt was made to account for this affect in the soil evaporation formulation (equation (5)) by adjusting the relative humidity in the pore space, h_R . Other studies have shown that it is necessary to modify the h_R algorithm in

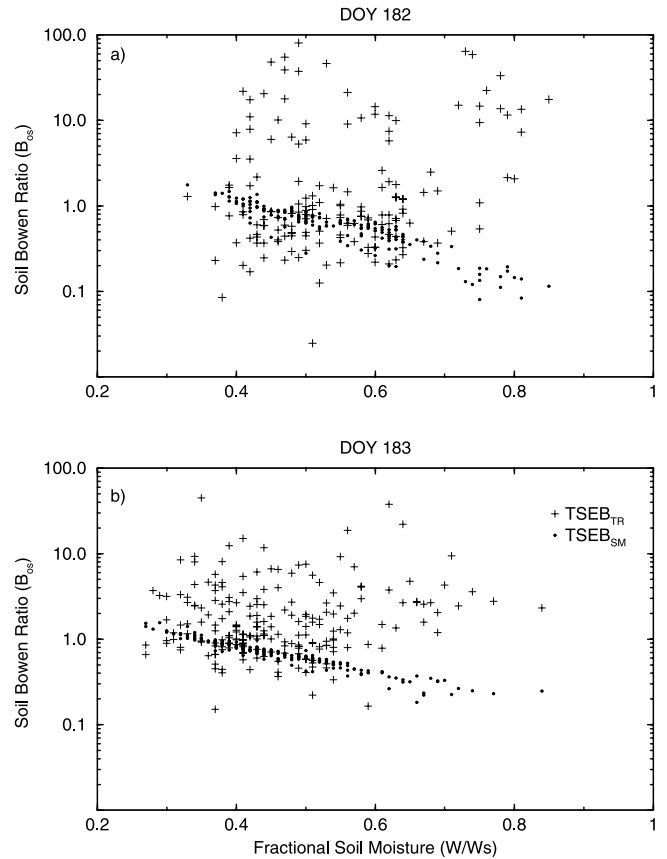


Figure 4. A semilog plot of the ratio of ESTAR-derived near-surface soil moisture, W , and saturated value, W_S , (W/W_S), versus soil surface Bowen ratios ($B_{OS} = H_S/LE_S$) from TSEB_{TR} and TSEB_{SM} output for a) DOY 182 and b) DOY 183 overpass.

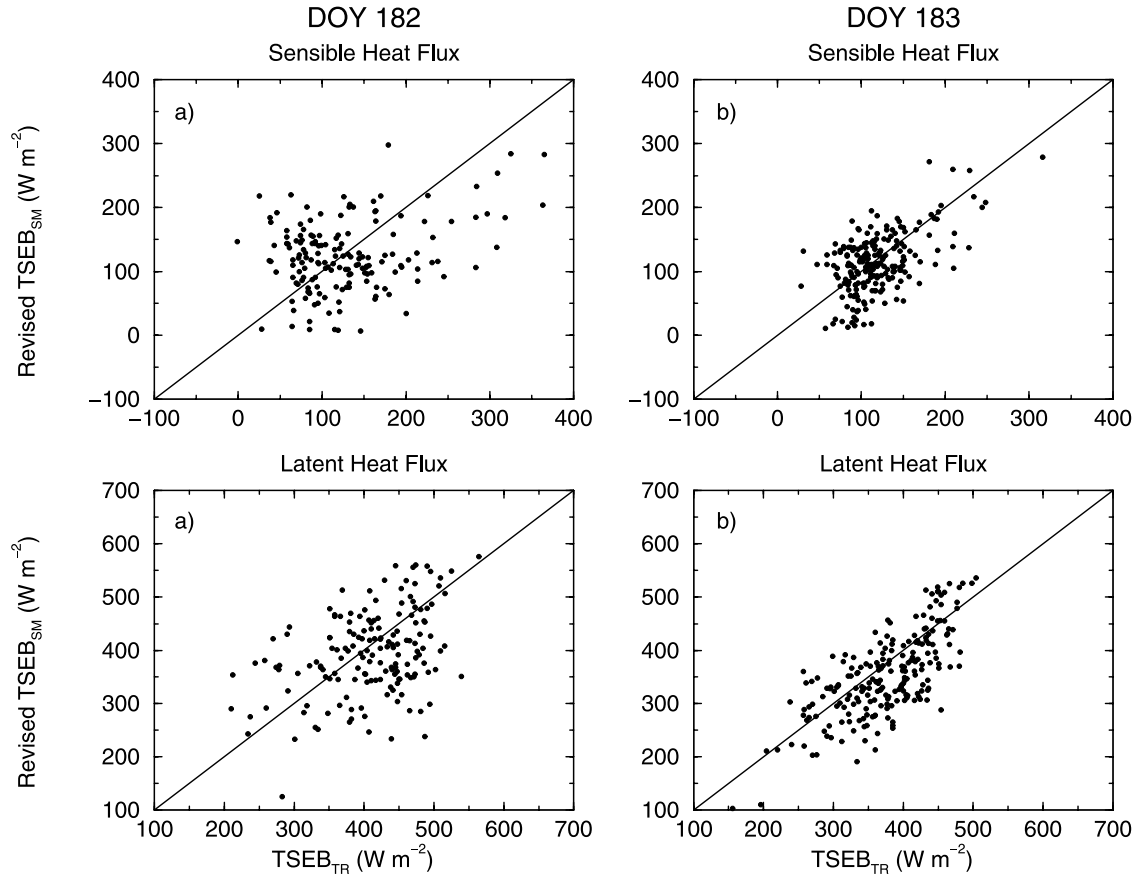


Figure 5. Comparison of sensible, (H), and latent (LE) heat fluxes between revised TSEB_{SM} scheme and the TSEB_{TR} formulation for a) DOY 182 and b) DOY 183 overpass.

order to obtain more reliable LE_S estimates [e.g., Cahill *et al.*, 1999]. This is due in part to the fact that value of h_R remains ~ 1 until the moisture is well below field capacity [Camillo and Gurney, 1986], and therefore does not account for the effect of differential drying in the near-surface soil layer. The adjustment was simply to multiply h_R in equation (5) by the ratio of the ESTAR-derived soil moisture, W , to the field capacity, W_{FC} , estimated from the soil texture database following Rawls *et al.* [1992]. In addition, since the TSEB_{SM} scheme cannot easily adjust α_{PT} in the Priestley–Taylor formulation, the TSEB_{TR} estimate of α_{PT} for each pixel is used by TSEB_{SM} in equation (6).

[20] The effect of these two revisions in the TSEB_{SM} output of the fluxes and T_{surf} is significant (Figures 5 and 6). The agreement between the two model estimates for both days has improved (cf. Figure 2) with RMSD for H and LE reduced to ≈ 75 W m⁻² and ≈ 85 W m⁻², respectively, for DOY 182. For DOY 183 the RMSD for H is reduced ≈ 40 W m⁻², while the RMSD remains at ≈ 60 W m⁻² for LE, but there is better overall agreement (Figure 5). The domain averages are also in much closer agreement, with $\langle H \rangle$ from TSEB_{SM} within 10 W m⁻² of the TSEB_{TR} estimate and $\langle LE \rangle$ within ≈ 20 W m⁻² of the TSEB_{TR} value for both days (Table 2). In addition for both days, the pixel-by-pixel comparison of T_{surf} simulated by TSEB_{SM} with $T_R(0)$ from TIMS shows little bias (Table 2) and with RMSD remaining at ≈ 3 K (Figure 6).

[21] The relationship between B_{OS} and W/W_S using the revised TSEB_{SM} model shows an increased sensitivity to near-surface soil moisture conditions compared to the original formulation (Figure 7), resulting in better agreement in the area-average B_{OS} , $\langle B_{OS} \rangle$ between the modeling schemes, particularly for DOY 183 (Table 2). However, there still remains little correlation between the B_{OS} values predicted by the two modeling schemes. This is primarily due to the fact that the TSEB_{SM} soil evaporation scheme (equation (5)) is strongly modulated by W/W_S via R_{SK} , hence the $B_{OS} - W/W_S$ relationship is highly correlated [Kustas *et al.*, 1998].

[22] Radiometric surface temperature is strongly coupled to the surface energy balance [Norman and Becker, 1995]. Therefore, one would expect that the TSEB_{TR} modeling framework would provide more accurate estimates of the heat fluxes than TSEB_{SM}. Yet, the significant decrease in the number of pixels having high B_{OS} values (i.e., $B_{OS} \geq 10$) as the soil surface dries indicates other factors are strongly affecting TSEB_{TR} output of energy partitioning at the soil surface. Since $\langle B_{OS} \rangle$ estimated from TSEB_{TR} increases over the two day period (Table 2), these other factors influence TSEB_{TR} model output only for particular areas/pixels in the image.

[23] A closer examination of the spatial distribution of B_{OS} for the two days along with W/W_S and NDVI maps for the study area (Figure 8) identifies areas where $B_{OS} \geq 10$, and provides insight into the factors most likely contributing to the differences in patterns of B_{OS} produced by the two

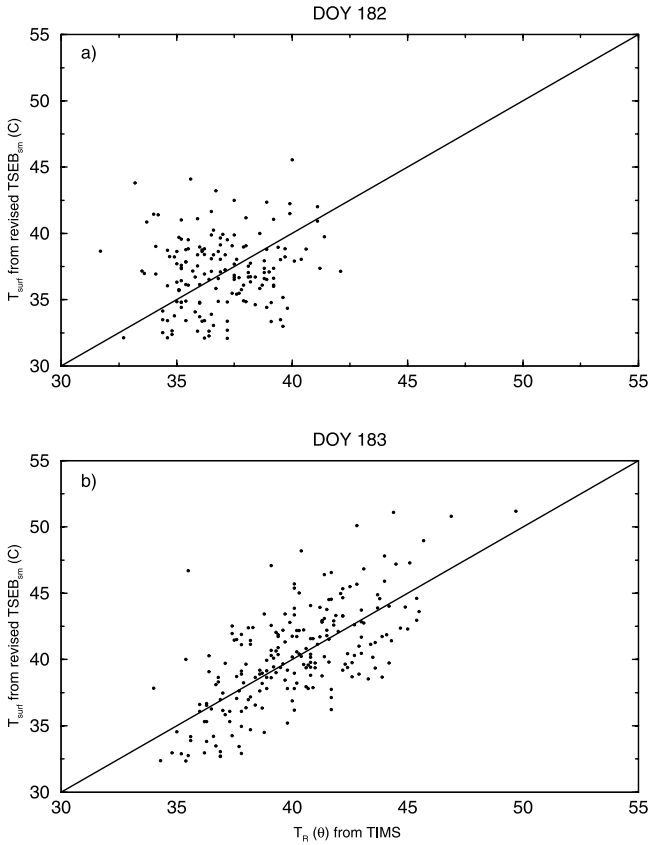


Figure 6. Comparison of effective surface temperature (T_{surf}) simulated by the revised TSEB_{SM} formulation versus remotely sensed (radiometric) surface temperature ($T_R(\theta)$) from the TIMS instrument for a) DOY 182 and b) DOY 183 overpass.

modeling schemes. For DOY 182, the wetter of the two days, B_{OS} values predicted by TSEB_{TR} are high even in areas where $W/W_S > 0.90$. Moreover, most regions where $B_{\text{OS}} \geq 10$ have relatively high NDVI, indicating a higher fractional vegetation cover (i.e., $f_C \geq 0.7$). A similar result from TSEB_{TR} output is produced for DOY 183, but there are significantly smaller areas having $B_{\text{OS}} \geq 10$ and where there are high B_{OS} values, their areal extent and location in many cases differs considerably from the previous day. This lack of consistency in the spatial patterns of B_{OS} values predicted by TSEB_{TR} for consecutive days indicates the energy partitioning at the soil surface in areas having high fractional vegetation cover is problematic. In contrast, the spatial pattern of B_{OS} from TSEB_{SM} is not as variable and the patterns of high and low B_{OS} are consistent for the two days with increasing B_{OS} values on the second, drier day.

[24] Area-average values of the canopy–air aerodynamic resistance, $\langle R_A \rangle$, and soil surface aerodynamic resistance, $\langle R_S \rangle$, for DOY 182 are respectively $\sim 1/2$ and $3/4$ of the magnitude computed on DOY 183 (Table 2). For the areas with $f_C \geq 0.7$, not only is $R_S \sim 3/4$ the magnitude (i.e., $R_S \sim 110 \text{ s m}^{-1}$ for DOY 182 versus $\sim 145 \text{ s m}^{-1}$ for DOY 183), but also $T_R(\theta)$ from TIMS is 37°C for both days. With nearly the same surface layer air temperature T_A (Table 1), this results in similar $T_R(\theta) - T_A$ values over the more densely vegetated cover areas for the two days. Since on

DOY 182 significantly lower aerodynamic resistances were estimated compared to DOY 183, high B_{OS} values for the densely vegetated areas are more likely to have been computed by TSEB_{TR} for this day, even though DOY 182 had higher near-surface soil moisture conditions.

[25] Another factor contributing to high B_{OS} values estimated by TSEB_{TR} for the densely vegetated areas is the remotely sensed fractional cover estimates computed via equations (2) and (3), which yield f_C values as high as ≈ 0.9 . With $T_R(\theta)$ from TIMS is $\sim 37^\circ \text{C}$ over the high cover areas and with the Priestley–Taylor assumption (equation (4a)) $T_C \approx T_A$, ($\sim 32^\circ \text{C}$), equation (1) computes a $T_S \approx 48^\circ \text{C}$, 55°C and 74°C for $f_C = 0.7$, 0.8 and 0.9 , respectively. For T_S values $\geq 55^\circ \text{C}$, it is found that the computed H_S via equation (4b) can exceed the available energy at the soil surface ($R_{\text{NS}} - G$) resulting in a nonphysical solution, namely $\text{LE}_S < 0$. This requires having a lower T_S value which is estimated by computing a higher T_C via adjustment to the Priestley–Taylor α_{PT} coefficient in equation (4a) and then satisfying the radiative balance via equation (1) [Kustas and Norman, 2000a, 2000b; Kustas et al., 2003]. By overriding the initial Priestley–Taylor parameterization (equation (4a)), T_C may end up being several degrees higher than T_A , which in turn could result in TSEB_{TR} model heat flux estimates indicating both dry surface soil moisture and stressed vegetation conditions.

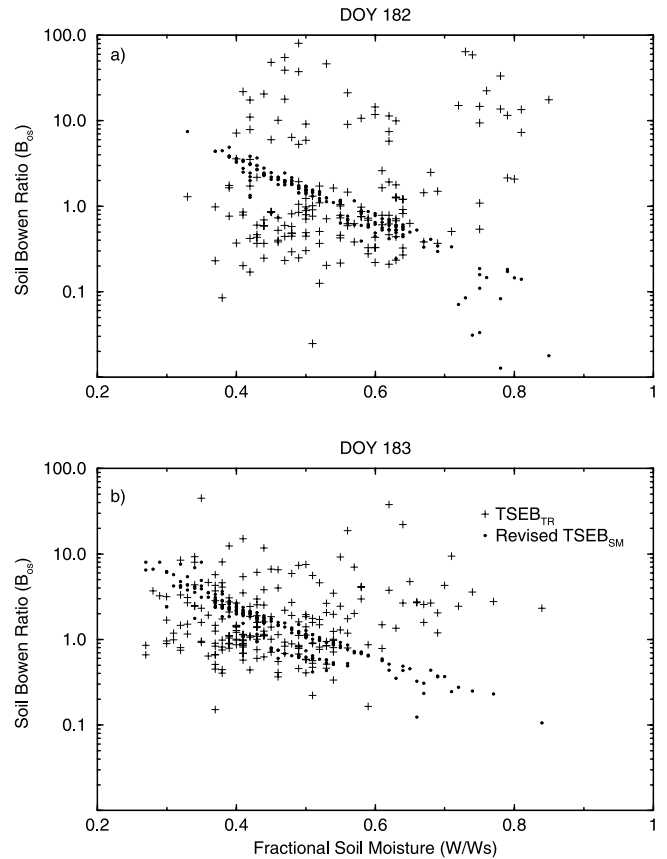


Figure 7. A semilog plot of the ratio of ESTAR-derived near-surface soil moisture, W , and saturated value, W_S , (W/W_S), versus soil surface Bowen ratios ($B_{\text{OS}} = H_S/\text{LE}_S$) from TSEB_{TR} and the revised TSEB_{SM} output for a) DOY 182 and b) DOY 183 overpass.

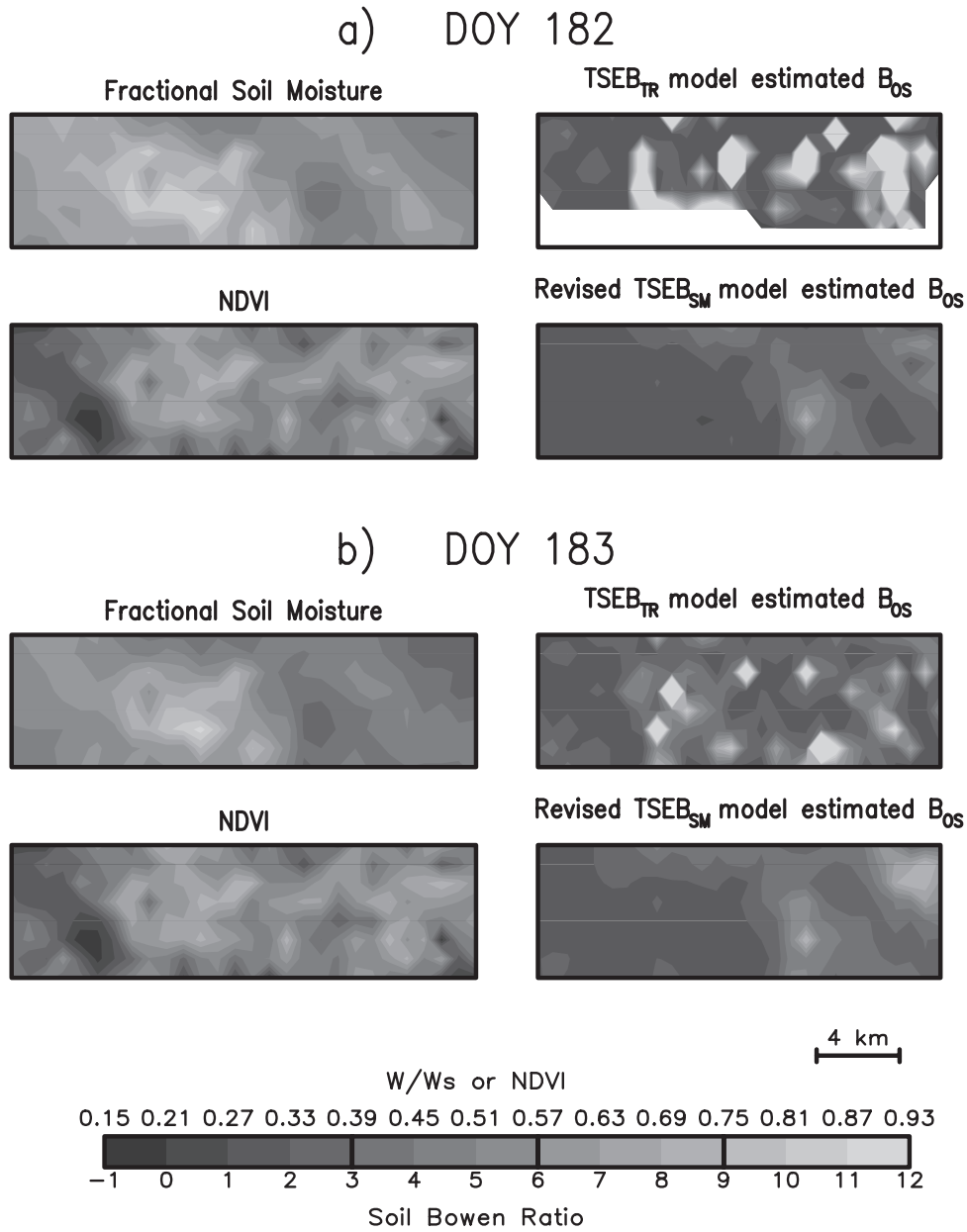


Figure 8. Spatial patterns of the ratio of ESTAR-derived near-surface soil moisture, W , and saturated value, W_s , (W/W_s), Normalized-Difference-Vegetation-Index (NDVI), and the soil surface Bowen ratios ($B_{OS} = H_S/LE_S$) from TSEB_{TR} and the revised TSEB_{SM} for a) DOY 182 and b) DOY 183 overpass. Note that white areas within the B_{OS} mapping area (delineated by the black border) indicate no output could be produced. This is due to the lack of radiometric temperature observations from TIMS for running TSEB_{TR}. See color version of this figure at back of this issue.

Table 3. Comparison of Area-Average Sensible, $\langle H \rangle$, and Latent Heat Fluxes, $\langle LE \rangle$, and Soil Surface Bowen Ratios, $\langle B_{OS} \rangle$, Estimated by the Two Models for Two Fractional Vegetation Cover Conditions, Namely the High Cover Case Where $\langle f_c \rangle \sim 0.5$ and the Lower Cover Case Where $\langle f_c \rangle \sim 0.4^a$

	Day 182				Day 183			
	TSEB _{TR} ($\langle f_c \rangle \sim 0.5$)	TSEB _{TR} ($\langle f_c \rangle \sim 0.4$)	TSEB _{SM} (Revised) ($\langle f_c \rangle \sim 0.5$)	TSEB _{SM} (Revised) ($\langle f_c \rangle \sim 0.4$)	TSEB _{TR} ($\langle f_c \rangle \sim 0.5$)	TSEB _{TR} ($\langle f_c \rangle \sim 0.4$)	TSEB _{SM} (Revised) ($\langle f_c \rangle \sim 0.5$)	TSEB _{SM} (Revised) ($\langle f_c \rangle \sim 0.4$)
$\langle H \rangle$, $W m^{-2}$	131	111	126	125	119	106	113	121
$\langle LE \rangle$, $W m^{-2}$	407	414	393	379	374	373	351	326
$\langle T_{surf} \rangle$, $^{\circ}C$	—	—	37.1	37.9	—	—	40.3	41.5
$\langle B_{OS} \rangle$	0.89	0.68	1.04	1.09	1.25	0.82	1.31	1.30

^aSee text for details. In addition, listed are TSEB_{SM}-derived area-average surface temperatures, $\langle T_{surf} \rangle$, under the two fractional vegetation cover conditions.

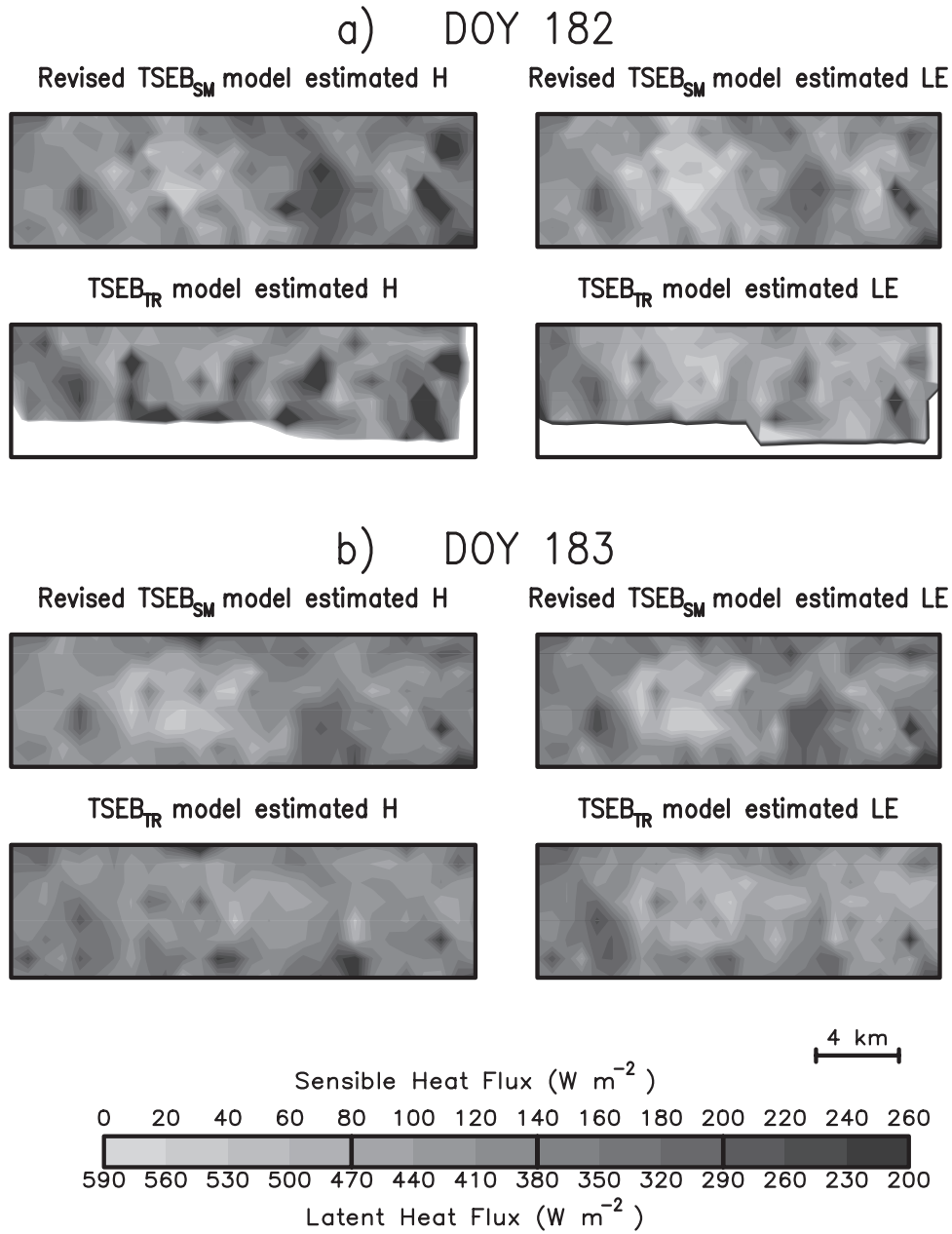


Figure 9. Spatial patterns of sensible (H) and latent (LE) heat fluxes from TSEB_{TR} and the revised TSEB_{SM} using the original or higher $\langle f_c \rangle$ case (see text) for a) DOY 182 and b) DOY 183 overpass. Note that white areas within the heat flux mapping area (delineated by the black border) indicate no output could be produced. This is due to the lack of radiometric temperature observations from TIMS for running TSEB_{TR}. See color version of this figure at back of this issue.

[26] The area-average f_c , $\langle f_c \rangle \approx 0.48$ computed from equations (2)–(3) is higher than estimated with the 30-m pixel resolution $NDVI$ data from French *et al.* [2000] where $\langle f_c \rangle \approx 0.43$ [see Kustas *et al.*, 2001]. By changing $NDVI_m = 0.8$ in equation (3), the value of $\langle f_c \rangle$ becomes ≈ 0.40 , closer to and more consistent with the estimate using the 30-m pixel resolution $NDVI$ data. The change in $NDVI_m$ also reduces f_c values for the densely vegetated areas where a maximum f_c of ≈ 0.7 is computed. This adjustment, particularly to the upper limit in f_c has a dramatic impact on B_{OS} computed by TSEB_{TR}. There is a significant reduction in pixels with $B_{OS} \geq 5$ from $\approx 25\%$ to $\approx 5\%$ for

DOY 182 and from $\approx 10\%$ to $\approx 1\%$ for DOY 183. The change in the f_c range had a minor affect on TSEB_{SM} output of B_{OS} with essentially no change for DOY 182 ($\approx 1\%$) and from $\approx 6\%$ to 4% for DOY 183. For both days there is also a greater change (decrease) in $\langle B_{OS} \rangle$ estimated by TSEB_{TR} using the lower $\langle f_c \rangle$ case compared to $\langle B_{OS} \rangle$ derived by TSEB_{SM}, which essentially does not change (see Table 3).

[27] There are relatively minor deviations in area-average heat fluxes estimated by either model using the lower $\langle f_c \rangle$ case. The change in $\langle H \rangle$ is larger for TSEB_{TR} compared to TSEB_{SM} while the opposite is true for $\langle LE \rangle$ (Table 3). For TSEB_{TR} the change in $\langle H \rangle$ is $\approx 15\%$ and $\approx 10\%$ for DOY

182 and 183, respectively, and $\approx 1\%$ for $\langle LE \rangle$ for both days. For TSEB_{SM} the change in $\langle H \rangle$ is less than 5% and change in $\langle LE \rangle$ is less than 10%. There is virtually no change in RMSD values comparing heat fluxes from the two modeling schemes (not shown) using lower versus the original or higher $\langle f_C \rangle$ case. However, disagreement in area-average heat fluxes, and $\langle B_{OS} \rangle$ between the two modeling schemes increases using the lower versus higher $\langle f_C \rangle$ case, as well as a larger difference between $\langle T_{surf} \rangle$ computed by TSEB_{SM} and $\langle T_R(\theta) \rangle$.

[28] These differences must also be considered in the context of model sensitivity to typical uncertainties in the other key remotely sensed inputs, namely $T_R(\theta)$ ($\pm 1.5^\circ\text{C}$) and W ($\pm 30\%$) for the TSEB_{TR} and TSEB_{SM} schemes, respectively. These uncertainties can cause $\sim 25\text{--}30\%$ variation in heat flux estimates [Kustas and Norman, 1997; Kustas et al., 1998]. Hence differences in heat flux output between the modeling schemes as well as discrepancies between $\langle T_{surf} \rangle$ and $\langle T_R(\theta) \rangle$ under the lower $\langle f_C \rangle$ case listed in Table 3 still fall within the range of expected variation in model output due to uncertainties in these other key remotely sensed boundary conditions. The main impact of using the lower $\langle f_C \rangle$ case is primarily seen in the significant reduction in B_{OS} values computed by TSEB_{TR} over the more densely vegetated areas.

[29] It is also important to recognize that microwave observations are affected by the presence of vegetation, and reduce the sensitivity of ESTAR observed brightness temperatures to near-surface soil moisture, particularly for high vegetation cover conditions [Jackson et al., 1995; Bindlish and Barros, 2002]. Errors in retrieval of W are greater under higher near-surface soil moisture conditions, as it becomes difficult to distinguish between the vegetation and near-surface soil moisture signal. However, errors in W under high vegetation cover conditions are largely systematic, thus will not contribute to the significant scatter observed in the relationship between B_{OS} estimates from TSEB_{TR} and W/W_S (Figures 4 and 7).

[30] Even with significant differences in the magnitude and distribution of B_{OS} between the two models, the spatial patterns in the total heat fluxes, H and LE , from the revised TSEB_{SM} scheme and TSEB_{TR} using the higher $\langle f_C \rangle$ case for the two days are quite similar (Figure 9). This result is due in large part to the fact that the major discrepancies in B_{OS} occur mainly under higher fractional vegetation cover conditions, namely $f_C \gtrsim 0.7$, where the soil contribution to the total heat flux is relatively small.

[31] By adopting the α_{PT} values estimated from TSEB_{TR} for computing latent heat flux with TSEB_{SM} scheme via equation (6) there was a only slight improvement in the agreement since ~ 85 to 90% of the pixels had $\alpha_{PT} = 1.3$ (>90 to 95% of the pixels had $\alpha_{PT} \gtrsim 1$) for DOY 182 and 183, respectively. This indicates that the revision to the soil evaporation formulation for the TSEB_{SM} scheme (equation (5)) was not only primarily responsible for improving the agreement in flux estimates with TSEB_{TR}, but also virtually eliminated the bias in between simulated and remotely sensed surface temperature.

5. Conclusions

[32] This analysis comparing output on a spatially distributed manner from two land–atmosphere transfer schemes

(TSEB) linking two different remotely sensed boundary conditions provided a unique opportunity to evaluate uncertainty in model flux estimates on a pixel-by-pixel basis. The TSEB_{SM} scheme is revised based on the comparisons made with the TSEB_{TR} flux output and comparisons between the effective surface temperature T_{surf} simulated by TSEB_{SM} and $T_R(\theta)$ observations from TIMS. The revisions resulted in closer agreement in heat fluxes computed by the two models and better agreement between TSEB_{SM} simulated and remotely sensed (radiometric) surface temperature.

[33] However, there remain significant discrepancies in heat flux output between the two models. This is due in part to the inconsistencies in the heat flux estimates from the TSEB_{TR} scheme, primarily in the partitioning of the available energy at the soil surface under the higher fractional vegetative cover conditions. With a significant radiometric surface–air temperature difference under high fractional cover conditions (i.e., $f_C \gtrsim 0.8$), soil surface temperatures $\gtrsim 55^\circ\text{C}$ are computed which do not satisfy soil surface energy balance constraints. Under this condition, the TSEB_{SM} scheme might give more realistic H_S and LE_S estimates since the B_{OS} patterns are more consistent during the dry down (Figure 8).

[34] A change in the fractional vegetation cover algorithm, which produces a lower area-average value consistent with an estimate using 30-m pixel resolution data and yields a maximum fractional vegetation cover $f_C \sim 0.7$, results in a significant decrease in the number of B_{OS} values $\gtrsim 5$ estimated by the TSEB_{TR} scheme. With the lower fractional vegetation cover estimates, there is less than a 15% change in area-average heat fluxes, but differences in output between the two modeling schemes are greater compared to using the original fractional cover values. However, errors in other key model inputs, namely $T_R(\theta)$ and W , are likely to cause $\sim 25\text{--}30\%$ variation in heat flux estimates from the two modeling schemes. This is greater than the observed differences due to a change in fractional cover estimates. Therefore, the main impact of using lower fractional cover estimates is primarily seen in the significant reduction in B_{OS} values computed by TSEB_{TR} over the more densely vegetated areas. This result suggests that under certain environmental conditions, energy balance partitioning at the soil surface over densely vegetated areas may be tenuous using the TSEB_{TR} scheme.

[35] Future work will involve comparing the output from the two models using a higher resolution microwave-derived soil moisture product (~ 200 m pixel resolution) available for this study site [Jackson, 2001]. At 200 m resolution, pixels within individual fields under more uniform land cover conditions can be examined in detail. This will not only permit a model comparison of heat fluxes computed by TSEB_{TR} and TSEB_{SM} under more uniform pixel conditions, but also allow for direct comparison with tower-based flux observations since at this higher resolution, it is more representative of the source area contributing to the tower-based measurements [Kustas et al., 2001].

[36] **Acknowledgments.** This work was supported by the NASA EOS and Land Surface Hydrology Programs. In particular funding under NASA NRA 98-OES-11(Proposal order number S-10202-X) supported this research investigation. We are indebted to Tom Jackson for organizing and coordinating The Southern Great Plains 1997 Hydrology Experiment and

Ming Ying Wei of NASA Headquarters whose guidance and support made this project of greater value than its individual components.

References

- Bindlish, R., and A. P. Barros, Sub-pixel variability of remotely sensed soil moisture: An intercomparison study of SAR and ESTAR, *IEEE Trans. Geosci. Remote Sens.*, 40(2), 326–337, 2002.
- Brock, F. V., K. C. Crawford, R. L. Elliott, G. W. Cuperus, S. J. Stadler, H. L. Johnson, and M. D. Eilts, The Oklahoma Mesonet, a technical overview, *J. Atmos. Oceanic Technol.*, 12, 5–19, 1995.
- Cahill, A. T., M. B. Parlange, T. J. Jackson, P. O'Neill, and T. J. Schmugge, Evaporation from nonvegetated surfaces: Surface aridity methods and passive microwave remote sensing, *J. Appl. Meteorol.*, 38, 1346–1351, 1999.
- Camillo, P. J., and R. J. Gurney, A resistance parameter for bare soil evaporation models, *Soil Sci.*, 141, 95–105, 1986.
- Capehart, W. J., and T. N. Carlson, Decoupling of surface and near-surface soil water content: A remote sensing perspective, *Water Resour. Res.*, 33, 1383–1395, 1997.
- Choudhury, B. J., N. U. Ahmed, S. B. Idso, R. J. Reginato, and C. S. T. Daughtry, Relations between evaporation coefficients and vegetation indices studied by model simulations, *Remote Sens. Environ.*, 50, 1–17, 1994.
- Doriaswamy, P., A. J. Stern, and P. W. Cook, A classification technique for mapping biophysical parameters in the U.S. Southern Great Plains, in *Proceedings of the International Geoscience and Remote Sensing Symposium*, IEEE Cat. No. 007803-4403, pp. 862–865, Inst. of Electr. and Electron. Eng., Piscataway, N. J., 1998.
- French, A. N., T. J. Schmugge, and W. P. Kustas, Surface fluxes over the SGP site with remotely sensed data, *Phys. Chem. Earth, Part B*, 25, 167–172, 2000.
- Jackson, T. J., Multiple resolution analysis of L-band brightness temperature for soil moisture, *IEEE Trans. Geosci. Remote Sens.*, 39, 151–164, 2001.
- Jackson, T. J., D. M. LeVine, C. T. Swift, T. J. Schmugge, and F. R. Schiebe, Large area mapping of soil moisture using the ESTAR passive microwave radiometer in Washita '92, *Remote Sens. Environ.*, 53, 27–37, 1995.
- Jackson, T. J., D. M. LeVine, A. Y. Hsu, A. Oldak, P. J. Starks, C. T. Swift, J. D. Isham, and M. Haken, Soil moisture mapping at regional scales using microwave radiometry: The Southern Great Plains hydrology experiment, *IEEE Trans. Geosci. Remote Sens.*, 37, 2136–2151, 1999.
- Jiang, L., and S. Islam, Estimation of surface evaporation map over Southern Great Plains using remote sensing data, *Water Resour. Res.*, 37, 329–340, 2001.
- Kustas, W. P., and J. M. Norman, A two-source approach for estimating turbulent fluxes using multiple angle thermal infrared observations, *Water Resour. Res.*, 33, 1495–1508, 1997.
- Kustas, W. P., and J. M. Norman, Evaluation of soil and vegetation heat flux predictions using a simple two-source model with radiometric temperatures for partial canopy cover, *Agric. For. Meteorol.*, 94, 13–29, 1999.
- Kustas, W. P., and J. M. Norman, Evaluating the effects of sub-pixel heterogeneity on pixel average fluxes, *Remote Sens. Environ.*, 74, 327–342, 2000a.
- Kustas, W. P., and J. M. Norman, A two-source energy balance approach using directional radiometric temperature observations for sparse canopy covered surfaces, *Agron. J.*, 92, 847–854, 2000b.
- Kustas, W. P., X. Zhan, and T. J. Schmugge, Combining optical and microwave remote sensing for mapping energy fluxes in a semiarid watershed, *Remote Sens. Environ.*, 64, 116–131, 1998.
- Kustas, W. P., X. Zhan, and T. J. Jackson, Mapping surface energy flux partitioning at large scales with optical and microwave remote sensing data from Washita '92, *Water Resour. Res.*, 35, 265–277, 1999.
- Kustas, W. P., T. J. Jackson, A. N. French, and J. I. MacPherson, Verification of patch and regional scale energy balance estimates derived from microwave and optical remote sensing during SGP9, *J. Hydrometeorol.*, 2, 254–273, 2001.
- Kustas, W. P., J. M. Norman, T. J. Schmugge, and M. C. Anderson, Mapping surface energy fluxes with radiometric temperature, in *Thermal Remote Sensing in Land Surface Processes*, edited by D. A. Quattrochi and J. C. Luvell, Taylor and Francis, Philadelphia, Pa., in press, 2003.
- Mecikalski, J. R., G. R. Diak, M. C. Anderson, and J. M. Norman, Estimating fluxes on continental scales using remotely-sensed data in an atmospheric–land exchange model, *J. Appl. Meteorol.*, 38(9), 1352–1369, 1999.
- Norman, J. M., and F. Becker, Terminology in thermal infrared remote sensing of natural surfaces, *Remote Sens. Rev.*, 12, 159–173, 1995.
- Norman, J. M., W. P. Kustas, and K. S. Humes, A two-source approach for estimating soil and vegetation energy fluxes from observations of directional radiometric surface temperature, *Agric. For. Meteorol.*, 77, 263–293, 1995.
- Palluconi, F. D., and G. R. Meeks, *Thermal Infrared Multispectral Scanner (TIMS): An Investigator's Guide to TIMS Data*, JPL Publ. 85-32, Jet Propul. Lab., Calif. Inst. of Technol., Pasadena, Calif., 1985.
- Priestley, C. H. B., and R. J. Taylor, On the assessment of surface heat flux and evaporation using large-scale parameters, *Mon. Weather Rev.*, 100, 81–92, 1972.
- Rawls, W. J., L. R. Ahuja, D. L. Brakensiek, and A. Shirmohammadi, Soil water movement and infiltration, in *Handbook of Hydrology*, edited by D. R. Maidment, chap. 5, pp. 5.1–5.55, McGraw-Hill, New York, 1992.
- Sellers, P. J., M. D. Heiser, and F. G. Hall, Relations between surface conductance and spectral vegetation indices at intermediate (100 m² to 15 km²) length scales, *J. Geophys. Res.*, 97(D17), 19,033–19,059, 1992.
- Shafer, M. A., C. A. Fiebrich, D. S. Arndt, S. E. Fredrickson, and T. W. Hughes, Quality assurance procedures in the Oklahoma mesonet network, *J. Atmos. Oceanic Technol.*, 17, 474–494, 2000.
- Twine, T. E., W. P. Kustas, J. M. Norman, D. R. Cook, P. R. Houser, T. P. Meyers, J. H. Prueger, P. J. Starks, and M. L. Wesley, Correcting eddy-covariance flux underestimates over a grassland, *Agric. For. Meteorol.*, 103, 279–300, 2000.
- Willmott, C. J., Some comments on the evaluation of model performance, *Bull. Am. Meteorol. Soc.*, 11, 1309–1313, 1982.

R. Bindlish, Science Systems and Applications, Inc., Hydrology and Remote Sensing Laboratory, U.S. Department of Agriculture-Agricultural Research Service, Building 007 BARC-West, Beltsville, MD 20705, USA.

W. P. Kustas and T. J. Schmugge, Hydrology and Remote Sensing Laboratory, U.S. Department of Agriculture-Agricultural Research Service, Building 007 BARC-West, Beltsville, MD 20705, USA. (bkustas@hydrolab.arsusda.gov)

A. N. French, Hydrological Sciences Branch, NASA Goddard Space Flight Center, Code 974.1, Greenbelt, MD 20771, USA.

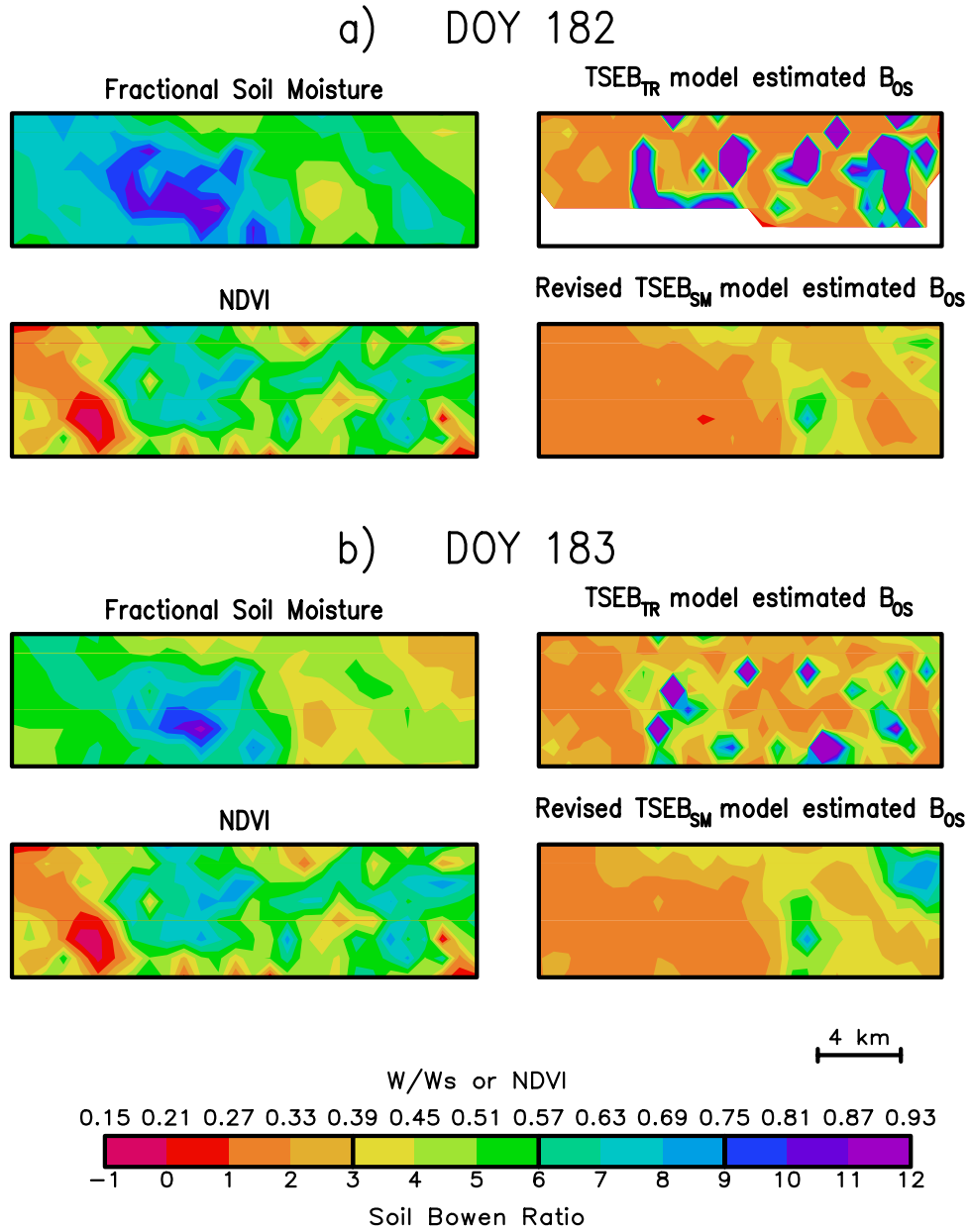


Figure 8. Spatial patterns of the ratio of ESTAR-derived near-surface soil moisture, W , and saturated value, W_s , (W/W_s), Normalized-Difference-Vegetation-Index (NDVI), and the soil surface Bowen ratios ($B_{OS} = H_s/LE_s$) from TSEB_{TR} and the revised TSEB_{SM} for a) DOY 182 and b) DOY 183 overpass. Note that white areas within the B_{OS} mapping area (delineated by the black border) indicate no output could be produced. This is due to the lack of radiometric temperature observations from TIMS for running TSEB_{TR}.

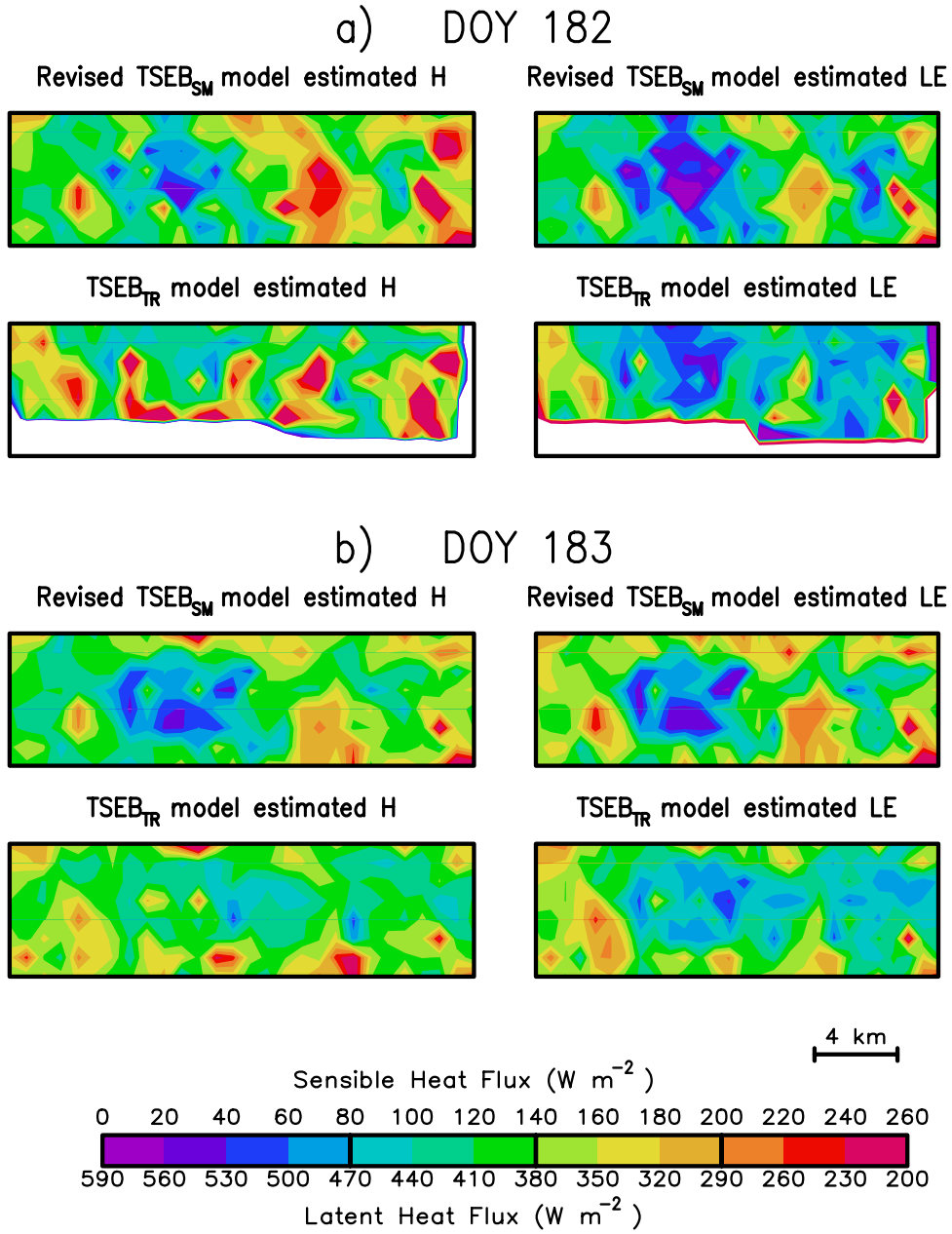


Figure 9. Spatial patterns of sensible (H) and latent (LE) heat fluxes from TSEB_{TR} and the revised TSEB_{SM} using the original or higher $\langle f_C \rangle$ case (see text) for a) DOY 182 and b) DOY 183 overpass. Note that white areas within the heat flux mapping area (delineated by the black border) indicate no output could be produced. This is due to the lack of radiometric temperature observations from TIMS for running TSEB_{TR}.